Journal of
Marine Science and Engineering

IMPACT FACTOR 2.9

CITESCORE 3.7

Article

A Simplified Experimental Method to Estimate the Transport of Non-Buoyant Plastic Particles Due to Waves by 2D Image Processing

Giovanni Passalacqua, Claudio Iuppa and Carla Faraci

MDPI

https://doi.org/10.3390/jmse11081599

Journal of *Marine Science and Engineering*

MDPI

Article

A Simplified Experimental Method to Estimate the Transport of Non-Buoyant Plastic Particles Due to Waves by 2D Image Processing

Giovanni Passalacqua, Claudio Iuppa * and Carla Faraci

Department of Engineering, University of Messina, Contrada di Dio, Sant'Agata, 98166 Messina, Italy; giovanni.passalacqua@studenti.unime.it (G.P.); carla.faraci@unime.it (C.F.)

* Correspondence: claudio.iuppa@unime.it

Abstract: Plastic is one of the most widely used materials. It is expected that there will be about 12 billion tons of debris dispersed into the environment by 2050. This, combined with marine littering, pollution and climate change will threaten our ability to sustainably use oceans, seas and coasts. In this regard, it is important to understand transport mechanisms and predict hotspots of plastic pollution. Physical models are a valid support to achieve such a goal. In this regard, it is necessary to adopt specific techniques which allow the movement of plastic to be monitored. Considering the relatively high size of plastic particles that could be used during experimental campaigns, new approaches based on image processing could be implemented. This study presents a simplified method to estimate the transport of particle debris under sea waves by 2D image processing, avoiding any disturbance of the dynamic field. The proposed method, based on the blob analysis, was implemented and calibrated within the wave flume of the Hydraulics Laboratory at the University of Messina. After a calibration process, the method was used to study the behaviour of the plastic debris under several hydrodynamic conditions. The results obtained in terms of displacement and velocity of the analysed sample showed a great reliability of the used methodology.

Keywords: plastic particles; non-buoyant particles; blob analysis; wind waves; plastics dynamics; cross-shore transport

Citation: Passalacqua, G.; Iuppa, C.; Faraci, C. A Simplified Experimental Method to Estimate the Transport of Non-Buoyant Plastic Particles Due to Waves by 2D Image Processing. *J. Mar. Sci. Eng.* **2023**, *11*, 1599. https://doi.org/10.3390/jmse11081599

Academic Editors: María Isabel Lamas Galdo and Georg Umgiesser

Received: 29 April 2023
Revised: 11 August 2023
Accepted: 14 August 2023
Published: 16 August 2023

1. Introduction

Pollution of the seas by plastic waste is one of the greatest environmental disasters of the last century. Since the end of World War II, humans have increased the production of plastic materials from the processing of fossil fuels, causing a major impact on our society [1]. It is difficult to identify an area of human activity that has not been influenced by plastic objects as they have characteristics that make them unique. Many products were built to serve only few minutes of usage but are destined to persist in the environment for hundreds of years. In this perspective, many of the plastic items become waste and most of them end up in the sea [2]. It was estimated that 275 million metric tons (MTs) of plastic waste were generated in 2010, with 4.8–12.7 MT turning out in the sea. Without improvements in waste management infrastructure, the amount of plastic waste entering the ocean from land is expected to increase by an order of magnitude by 2025 [3]. In recent years, the effect of micro-plastics in food chains, all the way down to humans, has also been tackled [4–6] with dramatic perspectives. The huge release of macro-plastic in the sea often leads to their fragmentation (due to the degradation phenomena), giving rise to a strong correlation between the ultimate fate of micro-plastics in the food chain and the original release of macro-plastic from urban areas to water bodies. It is therefore essential to invest in environmental management programs and, of course, in campaigns to remove plastics from the marine environment. In this regard, it is crucial to understand transport mechanisms and predict plastic pollution hotspots in the sea. However, few studies have

been performed so far on the dynamics of plastics in the marine environment and on the parameters that most influence the movement of debris [7–10]. It is worth pointing out that the major input of plastics (macro and micro) into the sea occurs via rivers [11]. During transport in rivers, plastics are exposed to various phenomena such as accumulation on the river bed and subsequent re-mobilisation [12]. When plastic waste arrives to the sea, it either gets trapped in shallow waters or is transported offshore and ends up in deep seas to the oceans as a consequence of the hydrodynamic phenomena.

The dominant hydrodynamics governing plastic particle transport in coastal waters significantly differ from the hydrodynamics that occur in the open ocean. The complex circulation patterns that control plastic transport on the onshore side of the marine shelf are largely influenced by wind, waves and tides, with the relative importance of water-depth-dependent forcings [13]. In addition to the hydrodynamic conditions, the dynamics of plastics, especially in coastal areas, are significantly influenced by the intrinsic properties of the particle, such as shape, size and density [14–17]. The density of plastics, which can be higher (non-buoyant plastics) or lower (buoyant plastics) than the density of water, is very important as it determines the drift they are subjected to.

The hydrodynamics that govern the motion of plastic particles in coastal areas are significantly affected by wind waves. In such areas, two main drifts can be generated: the longshore drift, which is dependent on the angle of incoming wave, and the cross-shore transport. With regard to the latter, the velocity profile established below the free surface is extremely complex. Its shape depends on the characteristics of both the waves and the seabed [18–20]. More specifically, water particles under waves are subject to both a predominant oscillating motion and a second-order steady flow called mass-transport [21]. Although the latter has a magnitude lower than the former, due to the persistence of the wave, it plays an important role in transport processes.

The net drift generated by such a mass-transport depends on the position of the plastic debris on the water column [16,22,23]. Generally, the particles floating on the free surface are subjected to a net drift in the direction of wave propagation known as Stokes drift. Such onshore mass-transport generates offshore flow known as mean return flow or undertow that may affect the suspended particles. At the bottom, the theoretical model of [21], valid for the horizontal bed, and the experimental campaigns conducted by [24] on a sloping bed show the generation of a net drift in the direction of wave propagation. In particular, they identified a forward flow at the bottom and at the surface (Stokes drift) and a backflow in the centre of the body of water (undertow). At the beaker zone, such flows are characterised by greater velocities.

In the present study, because the plastic density is greater than the density of the water (non-buoyant), the analysis is focused on the effects of the plastic transport close to the bottom with specific reference to the shoaling zone.

With regard to the study of the hydrodynamic effects of waves on particle displacement, several non-invasive approaches have been developed. For example, for sediment transport, specific methodologies were developed, and they are based on different techniques such as ultrasonic instrument system [25,26] or analysis of the images captured by a video camera [14,27–29].

With regard to plastic transport, in most of the experimental campaigns, the tracking of the position of the plastic debris is estimated by the post-processing of images acquired by a video camera. Alsina et al. [16] carried out experimental measurements of plastic particle drift in intermediate water depth. The displacements of the particle were sampled by means of two synchronized video–cameras with a resolution of 5.1 megapixels and a sampling frequency of 60–80 fps depending on wave conditions. The use of two synchronised video cameras allowed the authors to obtain the particle trajectories by using the stereoscopy concept. The calibration and the measures were carried out with the Openptv software. In Núñez et al. [30], 12 high-definition video cameras with a resolution of 2560 × 1440 pixels and a frame rate of 20 fps were used to monitor plastic transport along the wave flume in horizontal (eight cameras) and vertical (four cameras) directions.

The image processing was carried out by means of a Matlab algorithm which was used to estimate the cross-shore distribution concentrations. Guler et al. [31] studied the cross-shore distribution of non-buoyant micro-plastic particles under irregular waves. In their experiments, some runs were recorded using digital cameras placed outside the glass sidewalls of the flume. The recordings were used for video analysis of the behaviours of the particle under breaking conditions.

In the present study, a new methodology for tracking plastic debris transport within wave flumes is presented. The proposed approach, based on the analysis of the video recording through computer vision algorithms, was calibrated and verified at the Hydraulics Laboratory of the University of Messina. In particular, the transport of plastic particles (nylon) under different hydrodynamic conditions was investigated by processing the video frames using the blob analysis, i.e., a computer vision technique for the detection and analysis of connected pixels.

This study differs from the previously described studies since the proposed methodology allows a "continuous" tracking analysis to be performed rather than considering only the comparison of initial and final displacement conditions, as is often the case in other works.

The paper is organised as follows. The next section describes the algorithms for video recording processing. In Section 3, the laboratory equipment, wave conditions and plastic particle characteristics used in the runs are presented. Section 5 discusses the result of the validation activities and the results obtained from the proposed methodology. The last section reports some concluding remarks on the activity.

2. Video Recording Processing Algorithm

2.1. Algorithms for Frame Analysis

The video recording processing algorithm elaborates all the video frames in sequence. Each frame processing is performed through the sequential execution of algorithms necessary to detect plastic particles. Blob analysis, a main part of frame processing, is a technique for detecting the connected pixels in an image that differ in characteristics and properties from surrounding pixels [32]. This technique is used in various fields of engineering research [33–36]. However, to obtain the best performance of the blob analysis, it is necessary to carry out preliminary operations on the initial input image. The steps of the algorithms are the following: (i) split the video into individual RGB frames because the algorithms operate on single images; (ii) conversion from pixel coordinates to physical coordinates; (iii) transformation of RGB image into the binary image; (iv) detection of plastic particles.

The conversion from pixel coordinates to physical coordinates (step ii) is performed through a transformation matrix. Such a matrix is created using a Matlab function that processes the control point individuated on the unregistered image for which the coordinates in the metric system are known (Matlab function, ifitgeotform2d). The transformation of an RGB image into a binary image (step iii) allows a point or region to be easily detected in relation to its surroundings. Image thresholding is a simple but effective method of segmenting an image into the foreground and background [37]. This technique is a type of image segmentation that isolates objects by converting images (in any colour space) into binary (black and white) pictures. Working on the commands associated with the chosen colour space, it is possible to isolate the colour of the objects to be identified. This step is used to create the contrast mask according to the histogram thresholds chosen to export the binary image. In the last step (step iv), the binary image is provided to the blob analysis function. In particular, using a Matlab function (vision.BlobAnalysis) [38], it is possible to extract the properties of the blobs (area, coordinate of the centroid and bounding box of each blob). Such information can be used to monitor plastic debris displacement frame by frame. Figure 1 shows the workflow adopted for the frame-by-frame processing.

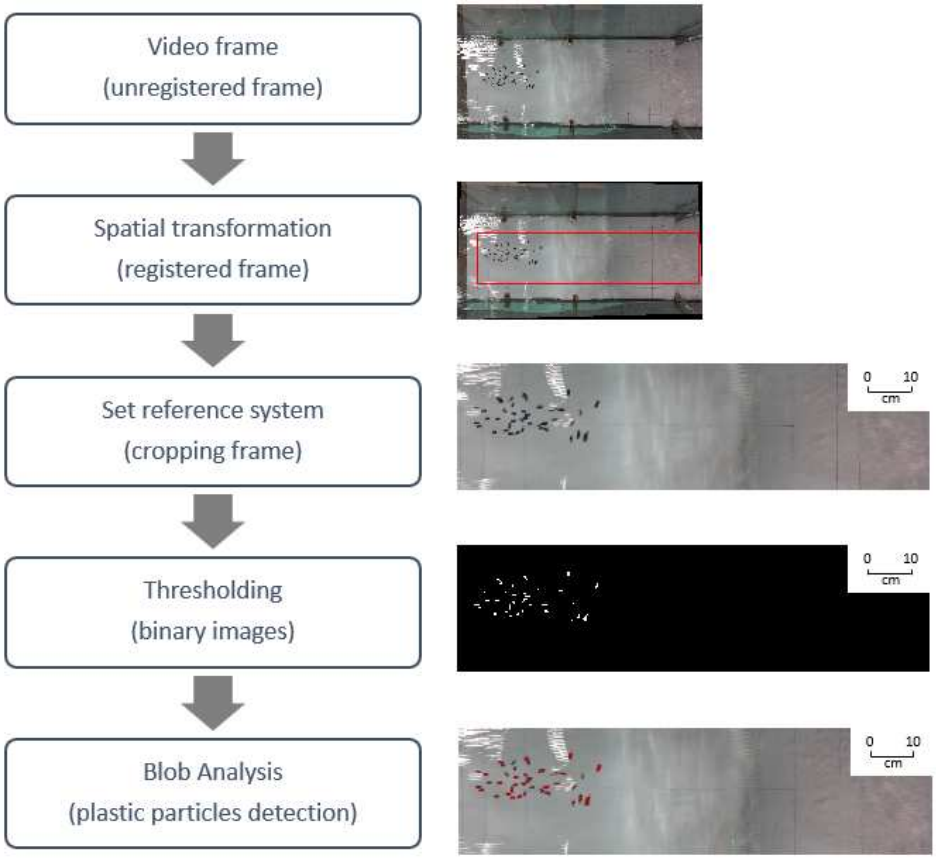

Figure 1. Workflow adopted for the processing of the video recording. The plastic particles used in the run are black. The red areas in the last image indicate the effective plastic debris detected by the blob analysis.

2.2. Characteristic Parameters of Plastic Debris Displacement

To track the advancement or retreat of the plastic particles laying on the bottom of the beach profile, a centroid representing the whole waste pattern was identified. This was performed by computing the centre of gravity of a system of masses, having previously calculated the coordinates of the individual centroids of the plastics using blob analysis. The output obtained from the blob analysis for each frame is a matrix of M lines (M equal to the number of objects identified) and 2 columns representing their x and y coordinates.

For each *k*-th object, the distance between it and the other identified objects is calculated using the following equation:

$$d_k = \sqrt{(x_j - x_k)^2 + (y_j - y_k)^2} \quad for\ j = 1, 2, 3, \ldots, M \tag{1}$$

The mean of the distances calculated with the previous formula is used to calculate the weight of each object compared to the others, using the equation:

$$m_k = \left(\frac{1}{d_{m,k}^2}\right) A_k \tag{2}$$

where: $d_{m,k}$ is the mean of the distances between the *k*-th object and the others; A_k is the area of the *k*-th object identified by the blob analysis. The estimation of the weight is conducted for the calculation of static momentums:

$$S_x = \sum y_k m_k \tag{3}$$

$$S_y = \sum x_k m_k \tag{4}$$

And finally, the coordinates of the barycentre of the system of objects are determined using the following equations:

$$X_g = \frac{S_y}{m_{tot}} \tag{5}$$

$$Y_g = \frac{S_x}{m_{tot}} \tag{6}$$

where m_{tot} indicates the sum of the weight of all objects.

The computation of the weight is performed to limit the weight of objects identified at an excessive distance from the rest of the ensemble. The formula in fact determines a mass inversely proportional to the square of the distance.

Finally, having determined the centroid of the set of particles for each frame and thus knowing the elapsed time, it is possible to estimate the distance covered by the centroid for each instant and thus the velocity as the ratio of distance to time.

In this work, this operation was performed for the whole plastic sample and for two other subsets of the global set of particles. It has been noted that due to the collision between the particles during movement, both due to the small turbulence occurring at the bottom (in the boundary layer) and due to the starting position of the individual element, the dynamic behaviour of the elements is not homogeneous; it is noted specifically that some particles tend to mobilise faster than others.

In this way, for each frame, the centroids of the particles that had x-coordinates higher (*up*) and lower (*down*) than the *global-centroid Xg*, called *up-centroid* and *down-centroid*, respectively, were determined. This allowed for not only the dynamic behaviour of the whole set of plastic particles, but also the extreme behaviour of particles that are more inclined to mobilisation (*up*) and more stationary (*down*), to be studied.

3. Experimental Procedure

3.1. Laboratory Equipment

Experiments were carried out within a wave flume which was 18.5 m long with a rectangular cross-section of 0.4 m × 0.8 m [39,40]. It was equipped at one end with a wave maker capable of generating regular and random waves (Figure 2a). The wave maker is of the flap type. The flap is pneumatically activated and electronically controlled by the Jonswap Wave Generator software. In the present campaign, however, only regular waves were generated and propagated in the flume.

On the opposite side of the wave flume, a sloped profile was built using steel panels with a first slope of 20% positioned approximately 8 m from the wave generator, followed by a 2.5 m long flat section and a second sloping area with a 20% slope created to simulate the gradual decreasing depth of the coastal zone. This area is framed by a video camera installed at the top, and it is composed by a first part with a variable slope called *slope A* and a second one with a fixed 20% angle called *slope B* (Figure 2b). The *slope A* part is comparable to a second-degree polynomial function characterised by the following equation: $y = 0.0001x^2 - 0.0005x$. This curved part was inserted to smoothen the transition from the flat to the sloping area.

The elevation, with respect to the horizontal bottom, of the summit point of the section with gradual change of slope is 2.8 cm. The depth at this point is indicated as $h*$, and it will be used further (Figure 2b).

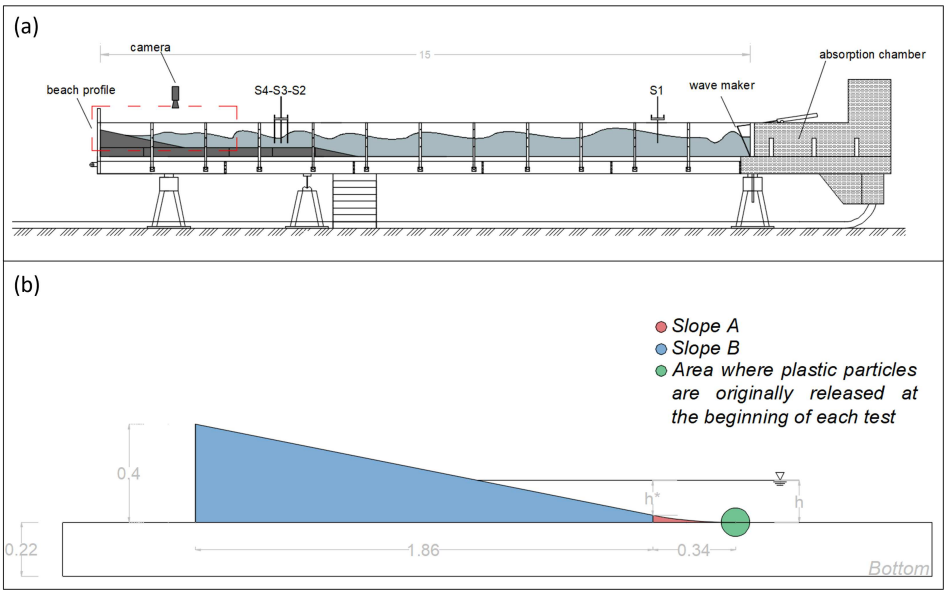

Figure 2. (**a**) General overview of the wave channel with framing of the level probes (S 1–4), video camera position and main components. (**b**) Closer view of the profile of the studied beach with the specification of the geometric lengths and identification of: Slope A in red, Slope B in blue and the point where the plastics are released at the beginning of each run in green. Dimensions are in metres.

A single camera with a resolution of 1920 × 1080 pixel, 30× zoom (4K), 28.8 mm wide angle lens, and a frame rate of 25 fps was used.

Four resistive wave gauges were positioned along the channel to measure the height of the free surface subject to wave motion: Three of them were positioned at a relatively short distance from the observation site to determine the reflection coefficient, which was evaluated using the three probe method of Mansard and Funke [41]; the fourth was positioned close to the wave maker so that the wave height could be measured offshore. With respect to the wave maker point, the probes were placed as follows: probe 1 at 2.15 m, probe 2 at 9.58 m, probe 3 at 9.77 m, and, finally, probe 4 at 9.88 m (Figure 2a). Wave data were recorded and processed using LabVIEW software. A Vectrino Profiler (Nortek As.) was used to measure fluid velocities. The Vectrino is composed of four beams that allow measurement of velocity components along the x-wave-propagation-direction, the transverse y-direction, and the vertical z-direction. Velocity measurements were acquired for each simulated wave condition. Velocity profiles were obtained along the same vertical section where plastics were released.

3.2. Plastic Particles

In this study, a sample of Nylon particles was tested; the particles were obtained from plastic waste and divided into small pieces of 10 mm × 5.4 mm × 1.1 mm. The *Corey shape factor* (csf) is equal to 0.15, denoting substantially flat particles [42]. The density was estimated by hydrostatic balance and resulted to 1.15 g/cm^3, higher than water density.

The sample was intentionally chosen from dark-coloured (black) waste to contrast with the white background to facilitate computer vision operations (Figure 3). The samples created were chosen with density and dimensions common to plastic waste readily found in seas and oceans [43,44].

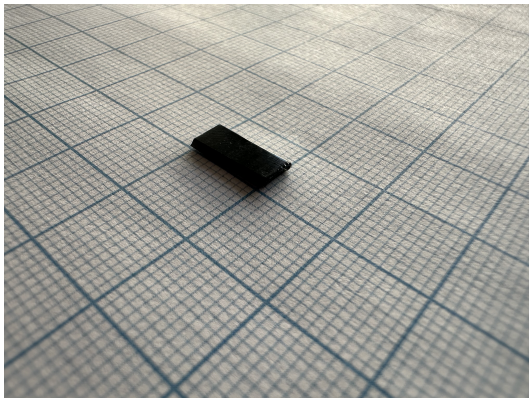

Figure 3. Sample of nylon plastic particles with *Corey shape factor* of 0.15 and density of 1.15 g/cm^3.

4. Experiments

The experiments were conducted by analysing 3 different water depths h: 0.23 m, 0.18 m and 0.15 m, measured at the point where the plastic particles are released, i.e., 0.22 m above the bottom of the flume (see Figure 2b). For each depth configuration, six wave conditions were tested, varying the period T between 1.00 and 1.67 seconds; the wavelength L, calculated using the dispersion relation, between 1.140 m and 2.442 m; the wave height H_i between 0.022 m and 0.120 m; and the number of released plastic particles (20, 40 and 80). For each configuration, the reflection coefficient k_r was calculated. The parameters considered for the first six runs are shown in Table 1.

Table 1. Simulated conditions for the first six runs carried out with 20 particles at a depth of 0.23 m are shown: name of the run, number of incoming plastic particles, water depth at the initial point (h), wave period (T), wavelength (L), incident wave height (H_i) and reflection coefficient (k_r).

Run Name	*Particles Number*	h [m]	T [s]	L [m]	H_i [m]	k_r [-]
W_1	20	0.23	1.66	2.442	0.036	0.264
W_2	20	0.23	1.25	1.751	0.066	0.175
W_3	20	0.23	1.00	1.306	0.105	0.167
W_4	20	0.23	1.66	2.442	0.036	0.378
W_5	20	0.23	1.25	1.751	0.078	0.155
W_6	20	0.23	1.00	1.306	0.119	0.178

The ranges of the quantities described above are shown in Table 2 for each configuration.

Table 2. Simulated conditions: run name, number of input plastic particles, water depth at initial point (h), range of values of wave period (T), wavelength (L), incident wave height (H_i) and reflection coefficient (k_r).

Run Name	*Particles Number*	h [m]	T [s]	L [m]	H_i [m]	k_r [-]
$W_{1–6}$	20	0.23	1.00–1.66	1.306–2.442	0.036–0.120	0.155–0.378
$W_{7–12}$	20	0.18	1.00–1.66	1.209–2.231	0.022–0.088	0.185–0.523
$W_{13–18}$	20	0.15	1.00–1.66	1.140–2.055	0.026–0.077	0.153–0.403
$W_{19–24}$	40	0.23	1.00–1.66	1.306–2.442	0.036–0.118	0.147–0.403
$W_{25–30}$	40	0.18	1.00–1.66	1.209–2.231	0.023–0.097	0.179–0.520
$W_{31–36}$	40	0.15	1.00–1.66	1.140–2.055	0.028–0.081	0.146–0.388
$W_{37–42}$	80	0.23	1.00–1.66	1.306–2.442	0.036–0.119	0.167–0.380
$W_{43–48}$	80	0.18	1.00–1.66	1.209–2.231	0.023–0.098	0.192–0.508
$W_{49–54}$	80	0.15	1.00–1.66	1.140–2.055	0.029–0.084	0.172–0.384

The considered configurations were selected from a wider range of preliminary tests carried out to estimate the most interesting hydraulic characteristics. Each run lasted about

two minutes, i.e., a time-lapse long enough to allow the plastic particle dynamics to evolve as well as an adequate number of waves to be considered for statistical analyses.

The reflection coefficients obtained from the experimental runs were compared with the empirical values derived using the formula of [45]:

$$k_r = tanh\left(a \cdot \xi_0^b \right) \tag{7}$$

where a and b in the case of a smooth surface are equal to $a = 0.16$ and $b = 1.43$ [45], and ξ_0 is the Iribarren parameter calculated as

$$\xi_0 = \frac{tg\alpha}{\sqrt{2\pi H_i / gT^2}} \tag{8}$$

where α is the angle of the slope near the free surface.

Figure 4 shows the comparison between the reflection coefficients obtained from the experimental runs and the value predicted by Equation (7) for smooth slopes.

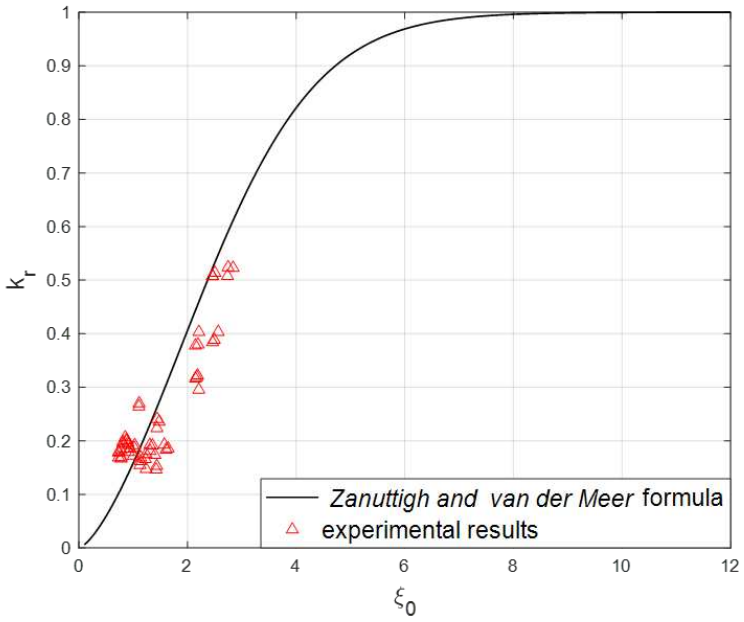

Figure 4. Comparison of the reflection coefficient obtained from experimentation (triangles) with the values obtained from Equation (7) for smooth slopes (line) as a function of Iribarren number.

The calculation of the reflection coefficient is important for estimating the influence of the reflected wave. In this case, the value of the reflection coefficient is between 0.14 and 0.5 and consistent with the values obtained by Equation (7).

5. Results

5.1. Flow Velocity

To characterise the hydrodynamics of both the flow and the plastic particles, different velocities were considered in this study, defined as follows: u indicates the instantaneous component of water velocity in the normal direction of the beach profile; U indicates the mass-transport velocity—that is, the mean value of u; U_S and U_L indicate the mass-transport velocity estimated according to Stokes and Longuet-Higgins theories, respectively; u_p and v_p indicate the instantaneous components of plastic centroid velocity in the normal and parallel directions of the beach profile, respectively; and U_p indicates the mean value of u_p.

Velocities measured with the Vectrino Profiler in the direction of wave propagation were considered. Measurements were taken along a vertical profile extending from the

smooth bottom up to an elevation of about 5 cm. As an example, a portion of the velocity signal acquired in wave direction (u), measured during a run with a depth of 0.23 m, a wave period of 1.25 s and a wave height of 0.12 m, is shown in Figure 5.

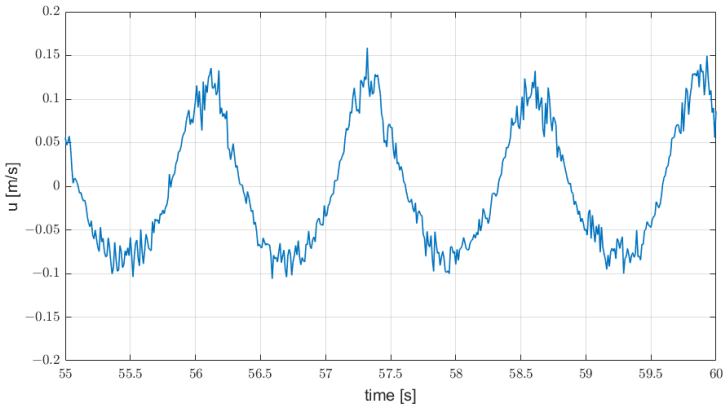

Figure 5. Representation of a small part of velocity signal in the wave direction (u) under the conditions of h = 0.23 m, T = 1.25 s, H_i = 0.12 m measured at the depth of 1.7 cm from the bottom.

For the same run, the time-averaged velocity profile (U) for each measurement point is shown in Figure 6. The mean profile reveals the existence of a reduced portion of the vertical column very close to the bed where the averaged velocity is directed onshore, giving rise to the existence of a net drift that drives the flow towards the coast [22]; from 1 cm above the bottom, the mean flow reverses, highlighting the presence of an undertow profile [21].

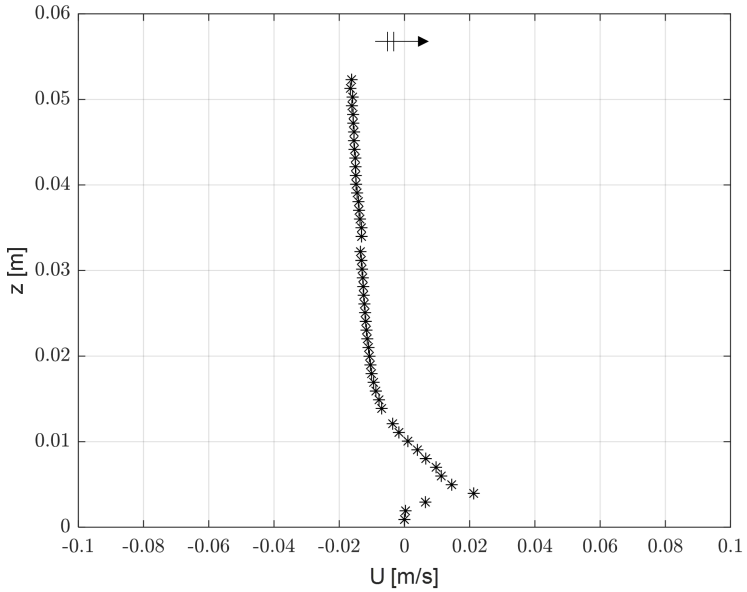

Figure 6. Time-averaged velocity profile (U) measured in the conditions of h = 0.23 m, T = 1.25 s, H_i = 0.12 m. The arrow indicates the direction of waves.

The net drift which was measured in the experiments can be related to the existence of a second-order mass-transport component found by Stokes [46] that can be expressed as

$$U_S = \frac{3}{16} H^2 \sigma k \frac{1}{sinh(kh)^4} \quad (9)$$

where $\sigma = 2\pi/T$ is the angular frequency of the wave.

However, later on, Longuet-Higgins [21] showed that the mass-transport can significantly differ from that predicted by Stokes, and he suggested the following formulation:

$$U_L = \frac{5}{4}\frac{a^2\sigma k}{sinh(kh)^2} \quad (10)$$

The plot in Figure 7 represents the comparison between the velocities measured during the experimentation with the Vectrino Profiler and the velocities estimated according to the Stokes [46] and Longuet-Higgins [21] theories.

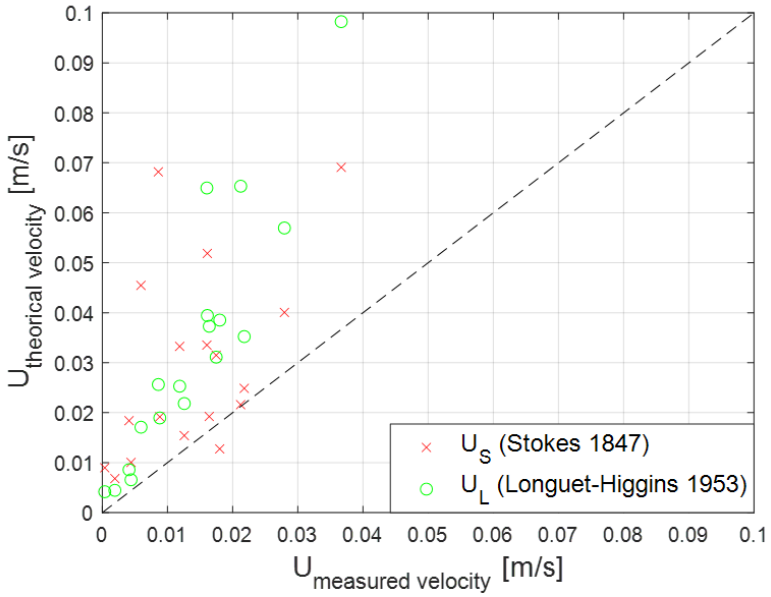

Figure 7. Comparison between the velocities measured during the experimentation with the Vectrino Profiler (U) and the velocities valued according to Stokes (U_S) and Longuet-Higgins (U_L) theories.

The comparison between the measured drift velocity at the elevation where it reaches its maximum (e.g., at z = 0.003 m with reference to the plot of Figure 6) and that estimated shows that both the two relationships overestimated the experimental values. Such differences are due to several reasons. The Stokes relationship is based on some assumptions (such as, for example, the slip condition on the bottom, the absence of the boundary layer, and the ideal fluid hypothesis) that restricted the theory to a limited number of cases. Although the Longuet-Higgins relationship is generally highly reliable for the prediction of the mass-transport velocity, it is based on a theory developed for a horizontal bottom far from the breaker zone. Due to the better correlation between measured drift velocities U and the Longuet-Higgins U_L estimation, in the following part of this paper, such a theoretical velocity will be considered to make the measured plastic velocities non-dimensional. In fact, as it will be detailed in the next sections, the net drift is basically the leading forcing that drives the movement of the plastic particles at the bed.

5.2. Validation of Spatial Transformation

First of all, in order to check their reliability, it was necessary to carry out validation procedures on the equipment and the methodologies to be applied. Regarding the first step of the algorithm used for image analysis, i.e., the procedure of spatial transformation from pixel coordinates to physical coordinates, transformation checks were carried out on representative frames. In particular, the aluminium plate used at the bottom of the flume was filmed from different perspectives. This step was repeated for seven different camera positions, varying both the height and angle of the camera with respect to the seabed. At this stage, several shapes of known dimensions were drown on the bottom

sheet aiming at acquiring at least 4 points (in the present case, 12 points were identified) as shown in Figure 8. Using the "projective" spatial transformation of the Matlab function $fitgeotform2d$ [38], the straight lines remain as such, but the parallel lines converge to a vanishing point.

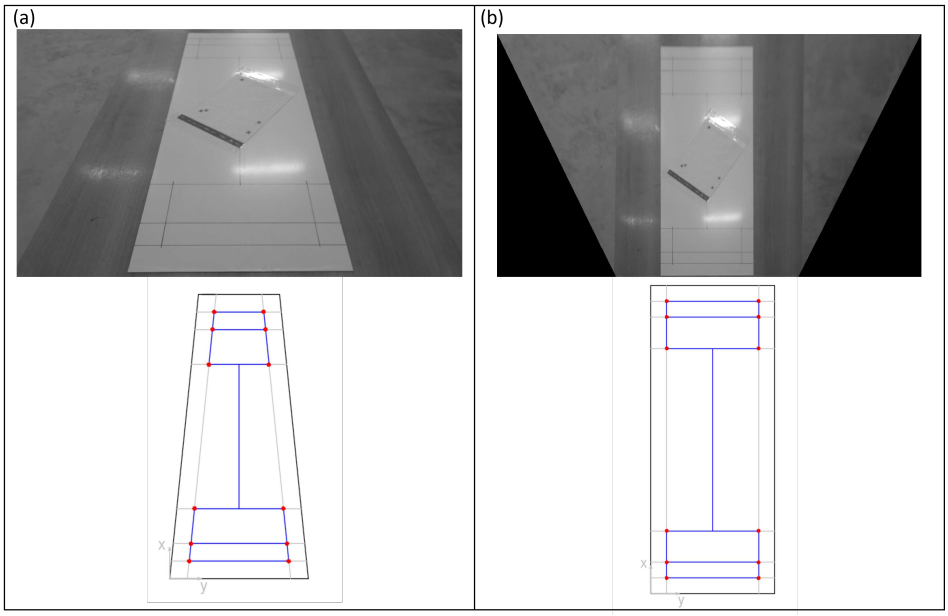

Figure 8. Example of an executed spatial transformation: the known points are sketched in red and the known distances are sketched in blue. (**a**) shows the original image and sketch, (**b**) shows the result after spatial transformation.

For each test, seven distance measurements were compared with the real dimensions. A maximum error of 1.55% and an average error of 0.44% were estimated. Based on the obtained result, the image transformation method adopted was considered to be fully efficient.

5.3. Calibration of Velocity Measurement

Several calibration tests were performed to calibrate the estimated velocities deduced from the particle tracking. Inside the flume, in a state of stillness without waves, a tray moving at a known constant velocity was filmed with a video camera (positioned at the same location as in the experiments). The tray was pulled by an electric engine rotating at a controlled speed. A number of plastic particles, with the same characteristics as those used in the experiments (see Figure 3), was glued on the surface of the tray; the displacement velocity of the centroid, identified with the blob analysis, was calculated over a known spatial range.

Comparing the results of the estimated speed obtained analytically as the time spent by the tray to travel a given space with those obtained from the blob analysis, it was noted that in the absence of wave motion, the velocities are similar; specifically, a maximum error between the two velocities of 3.17% was calculated (see Table 3 RUN $C_{1–4}$). On the other hand, comparing the results in terms of velocity for tests performed during wave propagation, the errors increase. Analyzing the images in detail, it was observed that the deformation of the water surface, caused by the waves, distorts the reading of the images and, consequently, the blob analysis.

In fact, it is noted that the diffraction of the images caused by the moving water has a significant impact on the determination of the displacements of the plastics' centroid in the considered time instants. To better calibrate the procedure, a test was performed in which the tray was filmed under wave action while keeping it stationary. In this way, the displacements detected by the blob analysis are only those that are due to the fictitious

displacement of the image diffraction generated by the passage of the waves but not corresponding to a physical motion of the particles. It was therefore necessary to analyse the power spectrum of the displacement signal as a function of its frequency and apply a filter to it to eliminate the noise causing the fictitious displacement. The filter used for the signal is a lowpass filter with a cutoff frequency equal to two times the frequency of the incident wave. The definition of the frequency value at which to truncate the power spectrum was not a simple operation, because by analyzing only the spectrum of the displacement signal, it was not possible to define which peaks correspond to the fictitious displacement. Considering that the motion of the plastic debris is mainly affected by the velocity field due to waves, the cutoff frequency was individuated by analysing the velocity signal acquired by a Vectrino Profile. In particular, the components of the velocity signal in the frequency domain with the higher power content were identified. As can be seen from Figure 9b, the frequencies with the higher power content are those lower than two times the frequency of the incident wave. Therefore, using the lowpass filter, it was possible to remove much of the noise due to the optical effect of image diffraction caused by waves passing over the surface. The residual part of the noise cannot be removed because the application of a filter with a bandpass frequency lower than the one considered would cause the removal of some of the displacement due to the waves themselves. Indeed, the drift which causes the displacement of the plastic particles is directly related to the second-order mass-transport velocity as evaluated in the previous section.

To estimate the error caused by residual noise, tests were carried out with the tray holding the samples pulled at a constant speed, but during wave propagation. The results in terms of velocity of the plastics sample (u_p) obtained analytically were compared with those estimated from the analysis with the application of the lowpass filter (see Table 3 RUN $C_{5–12}$).

The results displayed in Table 3 show that the maximum error obtained from these tests is 6.60%, and the average value stands at 2.64%. It is important to note that these error values incorporate errors due to the spatial transformation of images described in Section 5.2.

Table 3. Calibration of the plastics sample velocity (u_p) with analytically calculated values, values measured with blob analysis, error, standard deviation (SD) and test characteristics.

Run Name	*n° Particles*	*T* [s]	*Hi* [m]	*L* [m]	*Analytical Velocity* [m/s]	*Blob Velocity* [m/s]	Error [%]	*SD Velocity* [m/s]
C_1	1	-	-	-	0.027	0.027	2.13	0.003
C_2	1	-	-	-	0.056	0.054	2.74	0.004
C_3	8	-	-	-	0.053	0.052	1.99	0.003
C_4	8	-	-	-	0.050	0.048	3.17	0.002
C_5	1	1.25	0.05	1.60	0.060	0.058	2.93	0.015
C_6	1	1.00	0.08	1.21	0.077	0.760	1.13	0.032
C_7	1	1.25	0.06	1.60	0.054	0.053	0.82	0.021
C_8	1	1.00	0.09	1.21	0.061	0.059	1.99	0.039
C_9	8	1.25	0.05	1.60	0.049	0.048	2.37	0.027
C_{10}	8	1.00	0.07	1.21	0.049	0.048	0.34	0.038
C_{11}	8	1.25	0.06	1.60	0.048	0.045	4.94	0.027
C_{12}	8	1.00	0.09	1.21	0.059	0.054	6.60	0.061

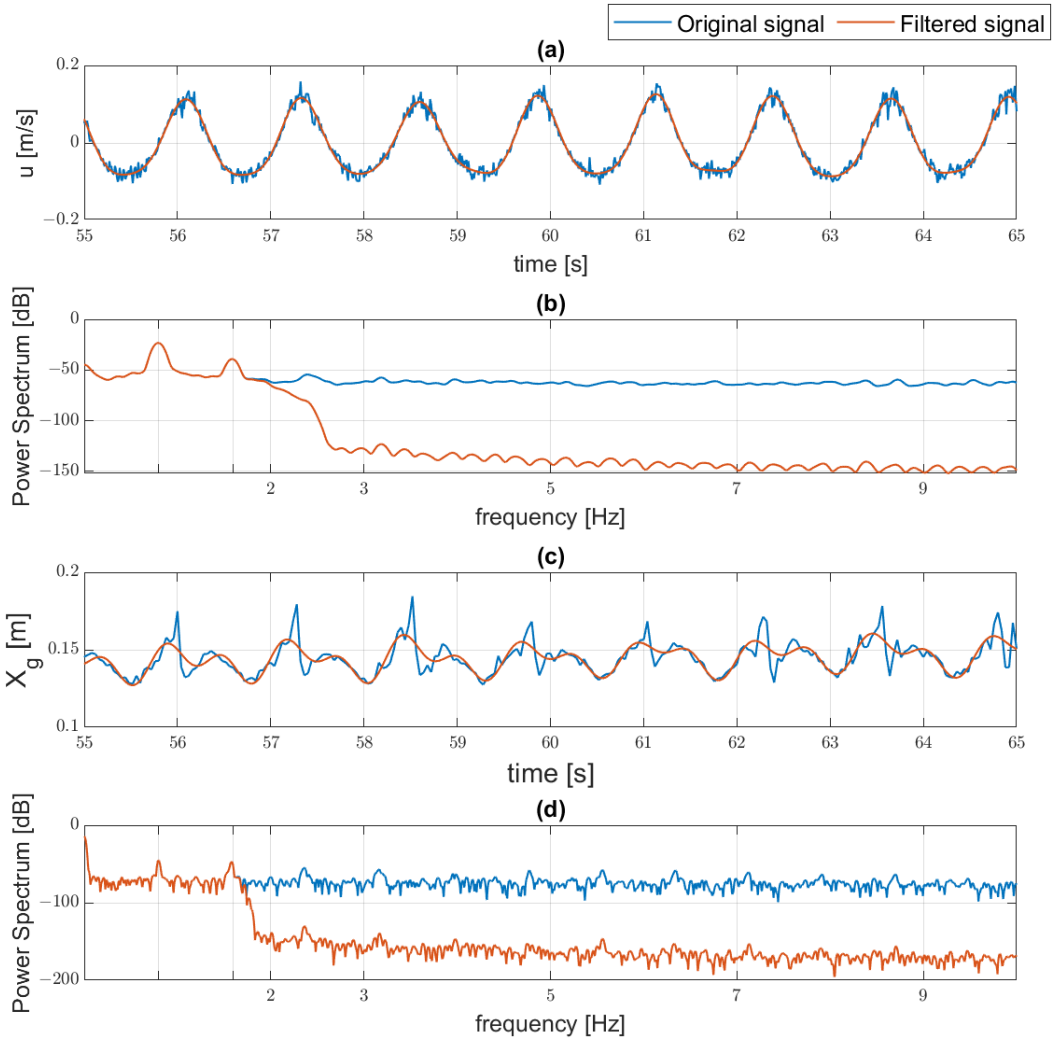

Figure 9. (**a**) Water velocity measurement (u) of original (in blue) and filtered (in orange) signals; (**b**) corresponding power spectrum of original (in blue) and filtered (in orange) signals. (**c**) *global centroid* (X_g) displacement of original (in blue) and filtered (in orange) signals; (**d**) corresponding power spectrum of original (in blue) and filtered (in orange) signals. RUN W_{53} h = 0.23 m, T = 1.25 s, H_i = 0.08 m.

5.4. Plastic Particles Velocity Analysis

Several physical parameters were extrapolated for each of the conducted runs. One of the most relevant quantities is the displacement velocity of the centroid of the plastic system subject to wave motion (u_p). During the runs, it was observed that as the wave motion characteristics change, the plastic sample expands and tends to approach the coastline over time, in accordance with the direction of the wave motion and in the presence of a second-order drift which is onshore directed, as shown in Figure 6. However, this movement is not uniform for each individual particle. In fact, thanks to the detailed analysis of the videos, it has been noted that some particles show a greater propensity to move than others; this can result in the rapid approach to the coastline and thus in the sucking of some elements in the breaking zone and, at the same time, the stalling of others in the input zone. For this reason, it was decided to describe the dynamic behaviour of the whole particle sample by the representation of its *global-centroid* and the behaviour of the sub-groups with the *up-centroid* and *down-centroid*, as described in Section 2.2.

Figure 10a shows the velocity variation in the x-direction (u_p), i.e., in the cross-shore direction of the centre of gravity of the plastic system over time.

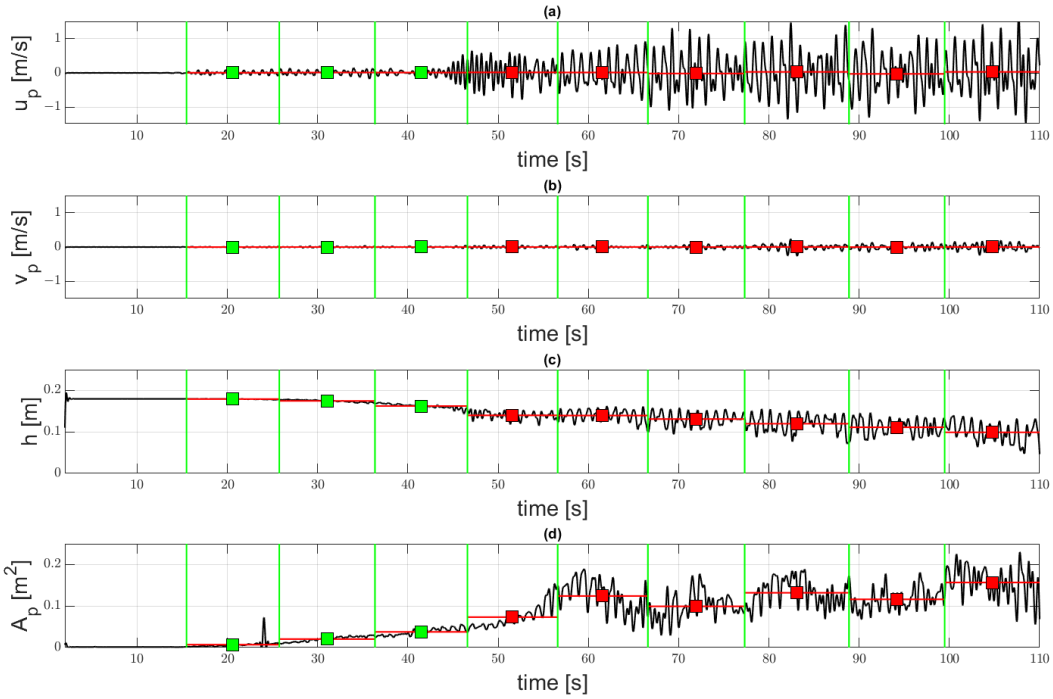

Figure 10. Temporal variation of the global-centroid physical characteristics: (**a**) velocity in the cross-shore direction (u_p); (**b**) velocity in the long-shore direction (v_p); (**c**) water depth; (**d**) area of the particles set. The green lines identify the phases for which there is a significant change in the mean of the velocity signal in the x-direction. For each phase, the mean value of the considered physical quantity was derived and identified with a square. The green square refers to the phases in which the up-centroid did not pass the breaking point; the red square indicates that the up-centroid passed the breaking point. The results refer to RUN W_{12} h = 0.18 m, T = 1 s, H_i = 0.088 m.

The number of data versus time is equal to the number of frames, while the 10 identified zones represent the phases in which the mean value of the velocity signal exhibits a significant variation. For each phase, the mean value of the velocity is calculated and superimposed to its time evolution. Moreover, the colour of the square reported on the plot for each average value depends on the location of the sample: more specifically, the phases identified by a red square indicate that the *up-centroid* (representative of the most advanced particles) has reached the breaking depth according to the Stokes criterion [47], while the green ones indicate that the breaker zone has not yet been reached by any of the moving particles.

Figure 10b shows the velocity change of the centroid of the plastic system in the y-direction (v_p), i.e., in the direction orthogonal to the wave propagation. It can be seen that this magnitude is much smaller than the x-directed one, thus confirming the two-dimensionality of the performed runs.

Figure 10c shows the change in the depth of the *global-centroid* of the plastic system as a function of time. Figure 10d shows the temporal variation of the area of a rectangle obtained as the product of the maximum distance between the objects (plastic particles) identified by the blob analysis in the x-direction and in the y-direction, i.e., a rectangular surface where the extremes on each side are the particles identified furthest from the centre of gravity in the two x- and y-directions. The variation of the area confirms what can be deduced from Stokes criterion when estimating the approaching of the *up-centroid* into the breaking zone. Indeed, a significant increase and subsequent decrease in the area indicate that some of the particles are moving very fast because they are being sucked in by the breaking wave. Hence, the oscillatory trend of such a parameter over time confirms that as far as the plastic sample enters the breaking zone, the blob analysis can no longer be applied.

Figure 11 shows the variation of velocity over time for the *global-centroid* (Figure 11a), the *up-centroid* (Figure 11b), and the *down-centroid* (Figure 11c).

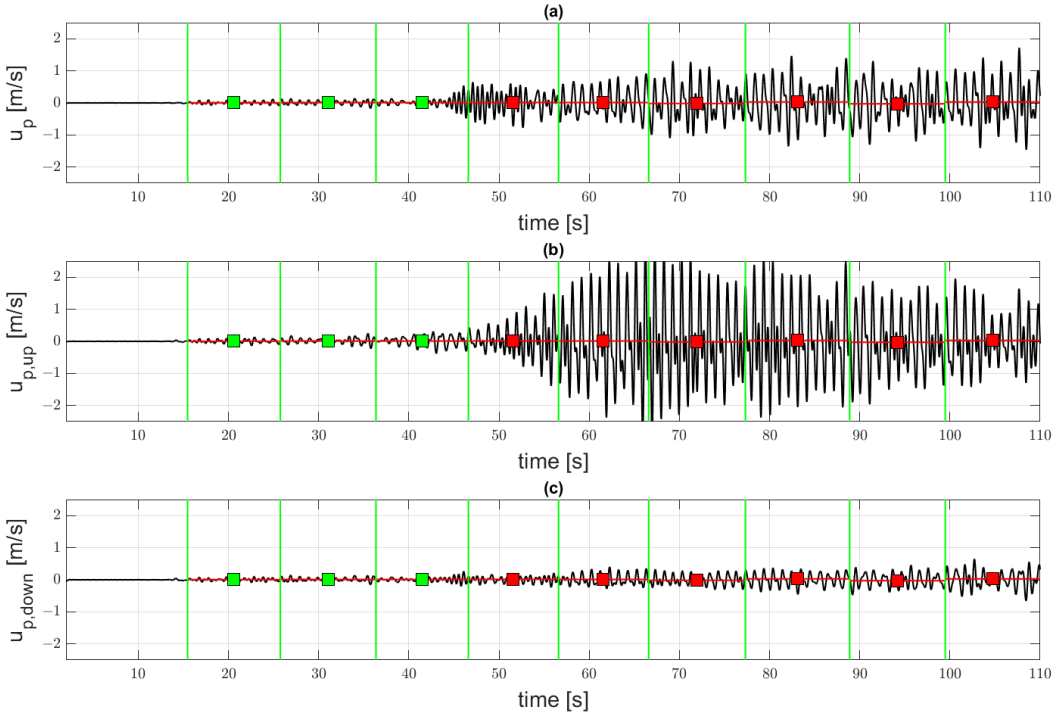

Figure 11. Temporal variation of velocities in the cross-shore direction of (**a**) global-centroid (u_p); (**b**) up-centroid ($u_{p,up}$); (**c**) down-centroid ($u_{p,down}$). The green lines identify the phases for which there is a change in the mean of the velocity signal in the x-direction. For each phase, the mean value of the considered physical quantity was derived and identified by a square. The green square refers to the phases in which the up-centroid did not pass the breaking point,the red square indicate that the up-centroid passed the breaking point. The results refer to RUN W_{12} h = 0.18 m, T = 1 s, H_i = 0.088 m.

For each identified phase, the velocity of the *up-centroid* ($u_{p,up}$) is greater than the other two, as the behaviour of the particles in the up-group is more inclined to mobilisation because these are the elements that avoid collisions with other particles. It can be seen that the first phase, in which an entry into the breaking zone is estimated (in this case, the fifth), is the one which shows the greatest increase in velocity. From that phase onwards, the velocity signal, as mentioned before, is influenced by the breaking process, and it is not relevant anymore to the aim of this present study.

In order to focus the time evolution of the centroids better, Figure 12 shows the frames corresponding to the mid-points of the phases identified in Figure 11.

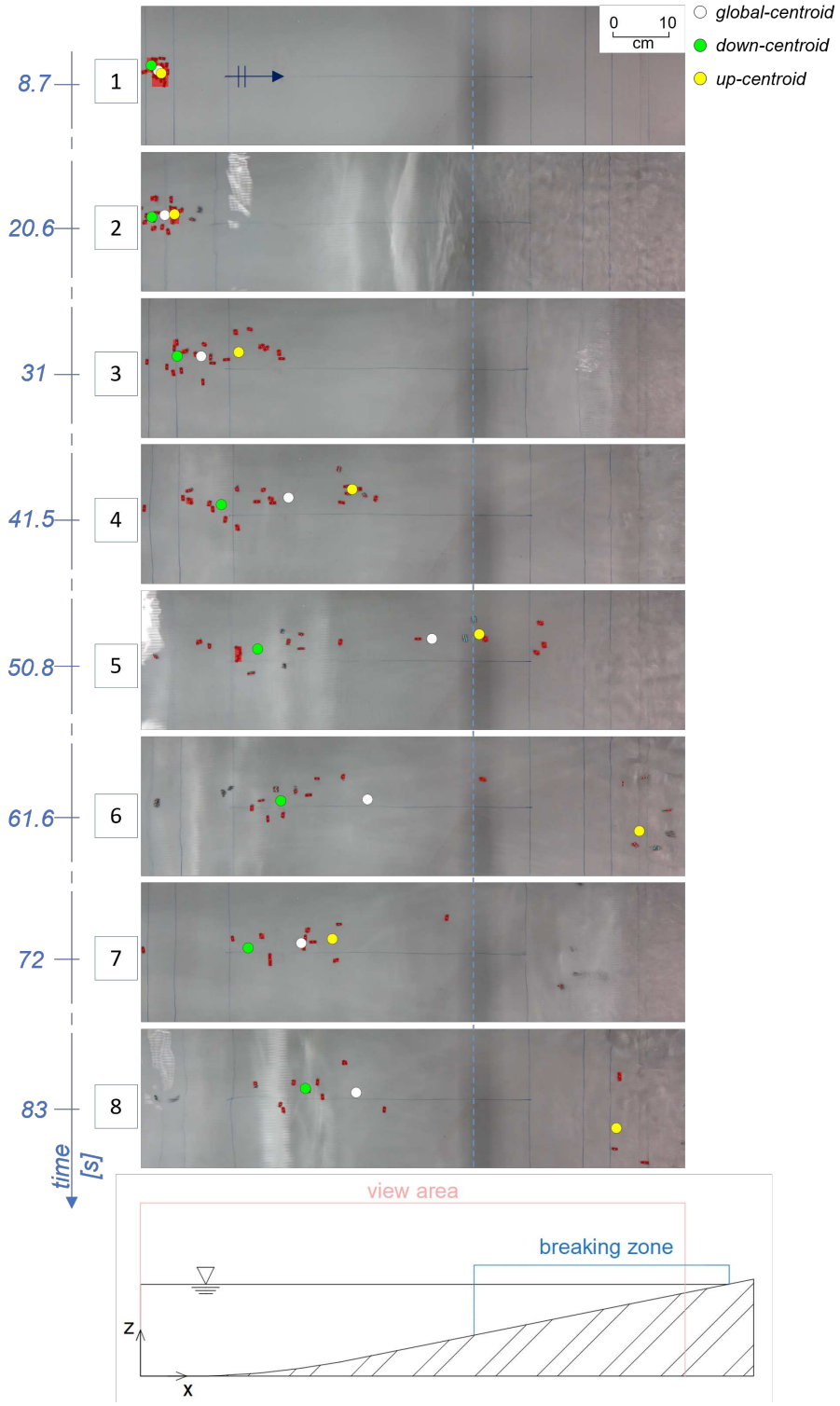

Figure 12. Frames of the first 8 phases of a run (RUN W_{12}) where the plastic particles are identified using blob analysis and where the global-centroid (white), the down-centroid (green) and the up-centroid (yellow) are marked with a point. The dashed blue line represents the transition into the breaking zone identified by the longitudinal profile of the shoreline shown below. The acquisition time in seconds is indicated for each phase.

It can be seen that in the first phase, the sample is stationary at the initial position; thus, this phase will be omitted from now onwards. During the second, third and fourth phases, distribution along the x-axis is observed and the breaking zone is reached. For the

run shown in Figure 12 (RUN W_{12}), the entry of the *up-centroid* into the breaking zone takes place at the fifth stage (Figure 11). From the sixth stage onwards, the identification of the *up-centroid* is complex because the most advanced particles fall into the swash zone and are hardly detected by the blob analysis.

Figure 13 shows the three averaged non-dimensional measured plastic sample velocities U_p/U_L, relative to the *down*, *global* and *up-centroid*, made non-dimensional with the second-order Longuet-Higgins velocity as a function of the product between the wave amplitude and wave number (ak). Each point corresponds to the mean of the results obtained for the phases preceding the breaking.

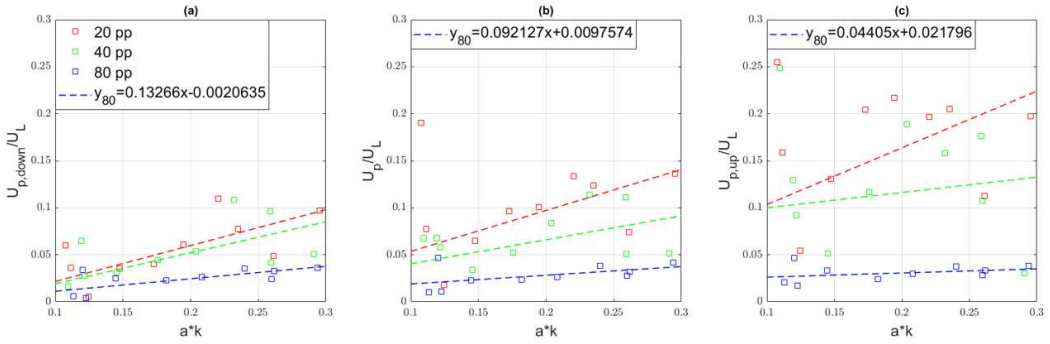

Figure 13. Dimensionless graphs comparing the product of wave amplitude and wave number and the ratio of the velocity measured in the cross-shore direction to the velocity estimated with Equation (10), in the case of: (**a**) down-centroid; (**b**) global-centroid; (**c**) up-centroid.

The comparison in Figure 13 shows the trends of the dimensionless parameters as the wave characteristics change (listed in Table 2) and as the number of input plastic particles varies for each run.

From the analysis of Figure 13, the effect of the wave steepness (ak) is evident. Indeed, as is known, mass-transport velocity tends to increase as the wave steepness increases. This is noticeable from Equation (10) which shows that the second-order velocity is directly proportional to the wave steepness. The consequence of this phenomenon is also that the velocity of the plastic debris increases as expected.

From the present experimental results, it is also evident that the number of plastic debris can influence the advancement velocity of the centroids. It can be observed for runs with 20 and 40 particles that, as the considered centroid changes, the slope of the trend lines varies, while it remains more or less constant for the sample of 80 particles. This happens because, during the initial phases, plastic debris located on the shoreline side (4–5 particles in our runs) is less subject to interaction with other particles. This implies that they move faster. The effect of these particles on the centroid velocity increases as the total number of particles decreases.

Similarly, Figure 14 shows the behaviour of the non-dimensional centroid depth, considered during the last phase before breaking, made non-dimensional by means of the depth at the beginning of the constant-slope section h^* (see Section 3.1), as a function of the product between the wave amplitude and the wave number.

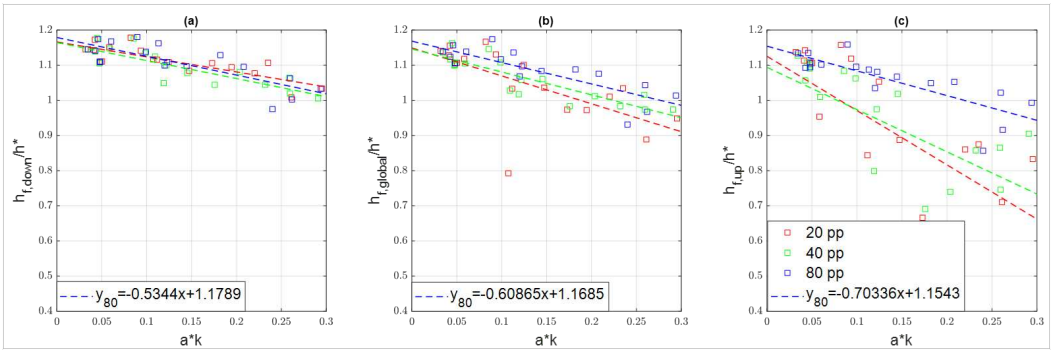

Figure 14. Dimensionless graphs comparing the product of amplitude and wave number and the ratio of the depth of the respective centroid at the last useful phase (before breaking rupture) to the depth at the start of the constant slope section with depth h*, in the case of (**a**) down-centroid; (**b**) global-centroid; (**c**) up-centroid.

As in the previous case, it is evident that the number of plastic samples influences the analysis, and the results appear to be less influenced by the behaviour of a single item when 80 particles are tested. Moreover, the analysis of Figure 14 reveals that values with ordinate greater than 1 do not pass the threshold of slope change. The infrequent passing of the crossing point between *Slope A* and *Slope B* is due both to the high slope of the last section (20%) and to the fact that the considered results relate to the mean of the phases preceding the breaking; thus, they matter for a limited time interval. This almost always occurs in the case of the *down-centroid* (Figure 14a) as it represents the rearmost group of particles. In the case of the *global-centroid* (Figure 14b), it can be seen that for high values of *ak*, the point of change of the slopes is exceeded; for the case of the *up-centroid* (Figure 14c), this occurs very often, especially for runs with 20 and 40 particles, as in this case, plastics are proportionally more easily transported towards the breaking zone.

6. Conclusions

The main objective of this work is to provide a contribution to the scientific community in the research area of the dynamics of plastic waste in the coastal zone. Attention is focused on the estimation of the velocities of given sets of elements by providing a simple and inexpensive experimental method.

The runs were conducted in a controlled environment, aiming at determining the displacements, velocities and distribution of the samples analysed using blob analysis. During the runs, different characteristics of wave motion, depth and number of sample elements were studied. A smooth beach profile consisting of sections with a variable slope was installed inside a wave flume. Each run was filmed using a video camera and each video was analysed by creating calculation codes using Matlab. The displacements and physical variables were estimated for each frame of each video; finally, the average values of the results were analysed and discussed. For each run, time-varying values of displacement, global velocity, velocity in x-direction, velocity in y-direction, depth and distribution were determined. Three centroids were identified from the dynamic behaviour of the plastic particles. Several difficulties were encountered during the experimental campaign: first and foremost, the calibration operations both to make the recorded images orthonormal and to reduce the error due to the fictitious shifts caused by the diffraction of the images during the passage of the waves occured. The results showed that blob analysis is a useful technique for studying the movements of sets of non-buoyant plastic particles until they fall into the breaking zone; they are then mobilised out of the camera frame. In this case, in fact, since the displacements were calculated in relation to the centroid of the set of particles, the disappearance and reappearance of some elements generate an error in the estimate of the displacement of the centroid. For this reason, the results obtained in the phases preceding the most advanced particle group reaching the breaking zone were considered accurate.

Different configurations of input particle numbers (20, 40 and 80) were tested during the runs, and it was observed that, especially in the initial stages of mobilisation, a small number of elements, about 4–5 for each run, moved faster than the rest of the group. The rapid advancement of these elements causes a significant impact on the average velocities of the centroids, especially when the number of input elements is relatively low. To study the dynamics of a group of plastic particles, it is therefore important to consider the potential effects of the number of tested elements.

Analysing the transport of plastic particles by progressive waves, a dependence of the plastic velocity U_p normalised with Longuet-Higgins second-order velocity U_L on wave steepness arises, showing the existence of a linear relationship of the type $U_p/U_L = c_1 \cdot a \cdot k.$, where the angular coefficient c_1 for the analysed case of 80 particles is about 0.1.

In addition, the non-dimensional depth at which the centroid stabilises before plastic particles enter the breaking zone decreases as the wave steepness increases, with a law of the type $h_f/h* = c_2 \cdot a \cdot k$, c_2 being about -0.6.

Notwithstanding, the present paper is mainly focused on the proposition of a novel technique and is aimed at its validation, calibration and testing; however, some insights on the transport of plastic debris can be promoted. Specifically, wave steepness seems to be a key parameter from the hydrodynamic point of view, being related to the second-order flow velocity. This means that for the performed experiments, the steeper the wave, the faster and further the non-buoyant debris will travel; this is different from what was surprisingly observed by Alsina and co-workers [16]. Future research will explore the dependence of these coefficients on morphological and physical parameters of different types of plastics and on different boundary conditions.

Author Contributions: C.I. and C.F. conceived of the presented idea. G.P., C.I. and C.F. conceived and planned the experiments. G.P. and C.I. carried out the experiment. C.I. and G.P. contributed to sample preparation. G.P., C.I. and C.F. contributed to the interpretation of the results. C.I. and G.P. wrote the manuscript with input from all authors. C.F. supervised the work. All authors have read and agreed to the published version of the manuscript.

Funding: This research was funded by the Italian MUR project PRIN2022 2022BCJ5W3—PLAstic Transport due to waves and currents ON Emerged and submerged beaches (PLATONE)—CUP J53D23002680006.

Institutional Review Board Statement: Not applicable.

Informed Consent Statement: Not applicable.

Data Availability Statement: The data presented in this study are available on request from the corresponding author.

Conflicts of Interest: The authors declare no conflict of interest.

References

1. Smith J.K., Jr. World War II and the transformation of the American chemical industry. In *Science, Technology and the Military*; Springer: Berlin/Heidelberg, Germany, 1988; pp. 307–322.
2. LI, W.C.; Tse, H.; Fok, L. Plastic waste in the marine environment: A review of sources, occurrence and effects. *Sci. Total Environ.* **2016**, *566*, 333–349. [CrossRef] [PubMed]
3. Jambeck, J.R.; Geyer, R.; Wilcox, C.; Siegler, T.R.; Perryman, M.; Andrady, A.; Narayan, R.; Law, K.L. Plastic waste inputs from land into the ocean. *Science* **2015**, *347*, 768–771. [CrossRef]
4. Ederer, B.; Sluka, R.D. Plastics in the Food Chain. *Perspect. Sci. Christ. Faith* **2020**, *72*, 169–170.
5. Amran, N.H.; Zaid, S.S.M.; Mokhtar, M.H.; Manaf, L.A.; Othman, S. Exposure to Microplastics during Early Developmental Stage: Review of Current Evidence. *Toxics* **2022**, *10*, 597. [CrossRef] [PubMed]
6. Klavins, M.; Klavins, L.; Stabnikova, O.; Stabnikov, V.; Marynin, A.; Ansone-Bertina, L.; Mezulis, M.; Vaseashta, A. Interaction between Microplastics and Pharmaceuticals Depending on the Composition of Aquatic Environment. *Microplastics* **2022**, *1*, 520–535. [CrossRef]
7. Critchell, K.; Lambrechts, J. Modelling accumulation of marine plastics in the coastal zone; what are the dominant physical processes? *Plast. Food Chain.* **2016**, *171*, 111–122. [CrossRef]
8. Zhang, H. Transport of microplastics in coastal seas. *Plast. Food Chain.* **2017**, *199*, 74–86. [CrossRef]

9. Van Sebille, E.; Aliani, S.; Law, K.L.; Maximenko, N.; Alsina, J.M.; Bagaev, A.; Bergmann, M.; Chapron, B.; Chubarenko, I.; Cózar, A.; et al. The physical oceanography of the transport of floating marine debris. *Environ. Res. Lett.* **2020**, *15*, 023003. [CrossRef]
10. Stocchino, A.; De Leo, F.; Besio, G. Sea waves transport of inertial micro-plastics: Mathematical model and applications. *J. Mar. Sci. Eng.* **2019**, *7*, 467. [CrossRef]
11. Lebreton, L.C.; Van Der Zwet, J.; Damsteeg, J.W.; Slat, B.; Andrady, A.; Reisser, J. River plastic emissions to the world's oceans. *Nat. Commun.* **2017**, *8*, 15611. [CrossRef]
12. Waldschläger, K.; Schüttrumpf, H. Erosion behavior of different microplastic particles in comparison to natural sediments. *Environ. Sci. Technol.* **2019**, *53*, 13219–13227. [CrossRef]
13. Lentz, S.J.; Fewings, M.R. The wind-and wave-driven inner-shelf circulation. *Annu. Rev. Mar. Sci.* **2012**, *4*, 317–343. [CrossRef]
14. Kerpen, N.B.; Schlurmann, T.; Schendel, A.; Gundlach, J.; Marquard, D.; Hüpgen, M. Wave-induced distribution of microplastic in the surf zone. *Front. Mar. Sci.* **2020**, *7*, 590565. [CrossRef]
15. Forsberg, P.L.; Sous, D.; Stocchino, A.; Chemin, R. Behaviour of plastic litter in nearshore waters: First insights from wind and wave laboratory experiments. *Mar. Pollut. Bull.* **2020**, *153*, 111023. [CrossRef]
16. Alsina, J.M.; Jongedijk, C.E.; van Sebille, E. Laboratory Measurements of the Wave-Induced Motion of Plastic Particles: Influence of Wave Period, Plastic Size and Plastic Density. *J. Geophys. Res. Ocean.* **2020**, *125*, e2020JC016294. [CrossRef]
17. Larsen, B.E.; Al-Obaidi, M.A.A.; Guler, H.G.; Carstensen, S.; Goral, K.D.; Christensen, E.D.; Kerpen, N.B.; Schlurmann, T.; Fuhrman, D.R. Experimental investigation on the nearshore transport of buoyant microplastic particles. *Mar. Pollut. Bull.* **2023**, *187*, 114610. [CrossRef]
18. Petrotta, C.; Faraci, C.; Scandura, P.; Foti, E. Experimental investigation on sea ripple evolution over sloping beaches. *Ocean. Dyn.* **2018**, *68*, 1221–1237. [CrossRef]
19. Faraci, C.; Scandura, P.; Petrotta, C.; Foti, E. Wave-induced oscillatory flow over a sloping rippled bed. *Water* **2019**, *11*, 1618. [CrossRef]
20. DiBenedetto, M.H.; Ouellette, N.T.; Koseff, J.R. Transport of anisotropic particles under waves. *J. Fluid Mech.* **2018**, *837*, 320–340. [CrossRef]
21. Longuet-Higgins, M.S. Mass transport in water waves. *Philos. Trans. R. Soc. London Ser. A Math. Phys. Sci.* **1953**, *245*, 535–581.
22. Scandura, P.; Foti, E.; Faraci, C. Mass transport under standing waves over a sloping beach. *J. Fluid Mech.* **2012**, *701*, 460–472. [CrossRef]
23. Pezerat, M.; Bertin, X.; Martins, K.; Lavaud, L. Cross-shore distribution of the wave-induced circulation over a dissipative beach under storm wave conditions. *J. Geophys. Res. Ocean.* **2022**, *127*, e2021JC018108. [CrossRef]
24. Bijker, E.; Kalwijk, J.T.; Pieters, T. Mass transport in gravity waves on a sloping bottom. In Proceedings of the 14th Conference on Coastal Engineering, Copenhagen, Denmark, 24–28 June 1974; pp. 447–465.
25. Turner, I.L.; Russell, P.E.; Butt, T. Measurement of wave-by-wave bed-levels in the swash zone. *Coast. Eng.* **2008**, *55*, 1237–1242. [CrossRef]
26. Saugy, J.N.; Amini, A.; De Cesare, G. Flow structure and grain motion assessments of large river widening in a physical model using ultrasonic Doppler velocity measurements. *Exp. Fluids* **2022**, *63*, 115. [CrossRef]
27. Radice, A.; Malavasi, S.; Ballio, F. Solid transport measurements through image processing. *Exp. Fluids* **2006**, *41*, 721–734. [CrossRef]
28. Liu, C.; Kiger, K.T. Multi-camera single-plane PIV imaging in two-phase flow for improved dispersed-phase concentration. *Exp. Fluids* **2022**, *63*, 41. [CrossRef]
29. Zimmermann, A.E.; Church, M.; Hassan, M.A. Video-based gravel transport measurements with a flume mounted light table. *Earth Surf. Process. Landf.* **2008**, *33*, 2285–2296. [CrossRef]
30. Núñez, P.; Romano, A.; García-Alba, J.; Besio, G.; Medina, R. Wave-induced cross-shore distribution of different densities, shapes, and sizes of plastic debris in coastal environments: A laboratory experiment. *Mar. Pollut. Bull.* **2023**, *187*, 114561. [CrossRef]
31. Guler, H.G.; Larsen, B.E.; Quintana, O.; Goral, K.D.; Carstensen, S.; Christensen, E.D.; Kerpen, N.B.; Schlurmann, T.; Fuhrman, D.R. Experimental study of non-buoyant microplastic transport beneath breaking irregular waves on a live sediment bed. *Mar. Pollut. Bull.* **2022**, *181*, 113902. [CrossRef]
32. Moeslund, T.B.; Moeslund, T.B. BLOB analysis. In *Introduction to Video and Image Processing: Building Real Systems and Applications*; Springer: Aalborg, Denmark, 2012; pp. 103–115.
33. Zhou, H.; Llewellyn, L.; Wei, L.; Creighton, D.; Nahavandi, S. Marine Object Detection Using Background Modelling and Blob Analysis. In Proceedings of the 2015 IEEE International Conference on Systems, Man, and Cybernetics, Hong Kong, 9–12 October 2015; pp. 430–435. [CrossRef]
34. Chen, T.H.; Lin, Y.F.; Chen, T.Y. Intelligent Vehicle Counting Method Based on Blob Analysis in Traffic Surveillance. In Proceedings of the Second International Conference on Innovative Computing, Information and Control (ICICIC 2007), Kumamoto, Japan, 5–7 September 2007; p. 238. [CrossRef]
35. Adal, K.M.; Sidibé, D.; Ali, S.; Chaum, E.; Karnowski, T.P.; Mériaudeau, F. Automated detection of microaneurysms using scale-adapted blob analysis and semi-supervised learning. *Comput. Methods Programs Biomed.* **2014**, *114*, 1–10. [CrossRef]
36. Jia, T.; Sun, N.l.; Cao, M.y. Moving object detection based on blob analysis. In Proceedings of the 2008 IEEE International Conference on Automation and Logistics, Qingdao, China, 1–3 September 2008; pp. 322–325. [CrossRef]
37. Al-Amri, S.S.; Kalyankar, N.V. Image segmentation by using threshold techniques. *arXiv* **2010**, arXiv:1005.4020.

38. *MATLAB*, version 9.13.0 (R2022b); The MathWorks Inc.: Natick, MA, USA, 2022.
39. Iuppa, C.; Carlo, L.; Foti, E.; Faraci, C. Calibration of CFD Numerical Model for the Analysis of a Combined Caisson. *Water* **2021**, *13*, 2862. [CrossRef]
40. Carlo, L.; Iuppa, C.; Faraci, C. A numerical-experimental study on the hydrodynamic performance of a U-OWC wave energy converter. *Renew. Energy* **2023**, *203*, 89–101. [CrossRef]
41. Mansard, E.P.; Funke, E. The measurement of incident and reflected spectra using a least squares method. In Proceedings of the 17th International Conference on Coastal Engineering, Sydney, Australia, 23–28 March 1980; pp. 154–172.
42. Corey, A.T. Influence of Shape on the Fall Velocity of Sand Grains. PhD Thesis, Colorado A & M College, Colorado State University, Fort Collins, CO, USA, 1949.
43. Mistri, M.; Infantini, V.; Scoponi, M.; Granata, T.; Moruzzi, L.; Massara, F.; De Donati, M.; Munari, C. Small plastic debris in sediments from the Central Adriatic Sea: Types, occurrence and distribution. *Mar. Pollut. Bull.* **2017**, *124*, 435–440. [CrossRef] [PubMed]
44. Sharma, S.; Sharma, V.; Chatterjee, S. Microplastics in the Mediterranean Sea: sources, pollution intensity, sea health, and regulatory policies. *Front. Mar. Sci.* **2021**, *8*, 634934. [CrossRef]
45. Zanuttigh, B.; van der Meer, J.W. Wave reflection from coastal structures in design conditions. *Coast. Eng.* **2008**, *55*, 771–779. [CrossRef]
46. Stokes, G.G. On the theory of oscillatory waves. *Trans. Cam. Philos. Soc.* **1847**, *8*, 441–455.
47. Dean, R.G.; Dalrymple, R.A. *Water Wave Mechanics for Engineers and Scientists*; World Scientific Publishing Company: Singapore, 1991; Volume 2.